Bulletin of the Seismological Society of America. Vol. 66, No. 2, pp. 385–404. April 1976

SOURCE PARAMETERS OF THE PT. MUGU, CALIFORNIA, EARTHQUAKE OF FEBRUARY 21, 1973

BY DAVID M. BOORE AND DONALD J. STIERMAN

ABSTRACT

Strong-motion recordings at Port Hueneme and Pasadena, at hypocentral distances of 24 and 80 km, respectively, have been fit with a number of commonly used dislocation models. The most satisfactory model is a fault in which rupture spreads circularly from the focal point (Savage, 1966). The derived model shows bilateral rupture with a lower bound on the moment of 1.5×10^{24} dyne-cm. With an assumed rupture velocity of 3.1 km/sec the stress drops are in the range of 50 to 200 bars. The moment of the initial rupture is well determined, but much uncertainty can exist in the other fault parameters. For example, if the rupture velocity is 1.55 km/sec, an equally good fit to the Port Hueneme record can be achieved, but a stress drop close to 4000 bars is required. The area of the initial rupture is smaller than the area outlined by the aftershock distribution. There is evidence in the Port Hueneme record that the rupture process involved a multiple earthquake, which would help explain the inconsistency between the initial slip area and the area shown by aftershocks. Studies of one-dimensional wave propagation through the sediments beneath the Port Hueneme station suggest that the surface motions have been amplified by a factor of about 2.8 compared with an equivalent bedrock recording, although the wave forms have not been distorted significantly. The observed motions were compensated for the effect of the sediments before the model fitting.

A comparison of different dislocation models shows that rupture propagation effects are important in fitting the observed motions and that if the finite extent of the rupture surface is accounted for, the ω^{-2} high-frequency decay of the displacement spectrum often attributed to the Haskell dislocation model should be closer to ω^{-3}.

INTRODUCTION

The Pt. Mugu, California, earthquake of February 21, 1973, was a moderately sized ($M_L = 6.0$) event with a focal depth (17 km) that is deep for California earthquakes. The complex aftershock pattern (Ellsworth *et al.*, 1973; Stierman and Ellsworth, 1976) does not outline a plane surface, and furthermore the aftershocks display a wide variety of focal mechanisms. Most aftershock hypocenters are separated from the main-shock focus by a region of low aftershock activity (Figure 1). A separation in the zones of most intensive seismicity has been observed in many main shock-aftershock sequences and is usually interpreted as defining the area of main-shock rupture. For this earthquake, however, source parameter studies of the Pasadena recording of the main shock indicated that the rupture area was considerably smaller than the zone outlined by the main shock and aftershocks (Ellsworth *et al.*, 1973; also see Figure 5a in Stierman and Ellsworth, 1976). We have made a new analysis of the source mechanism, using a different model of the source and, most importantly, using the strong-motion accelerograms recorded at Port Hueneme, which is within a focal depth of the earthquake and is separated in azimuth from Pasadena by 157° with respect to the epicenter. We confirm the smaller

area of the rupture as compared with the area defined by the aftershocks, but our estimates of the source parameters, although very uncertain, are generally higher than those in Ellsworth *et al.* (1973).

DATA

Although the Pt. Mugu earthquake was recorded on a number of strong-motion instruments in southern California (Maley, written communication 1975), the most important record for interpretation of the source mechanism was obtained at Port Hueneme, 24 km from the hypocenter. The next closest recording was at least 50 km away. The close epicentral distance (16 km) and the relatively deep focus by California standards (17 km), help in justifying the common modeling assumption of straight travel paths unaffected by geology. We assume that head waves, wide angle reflections,

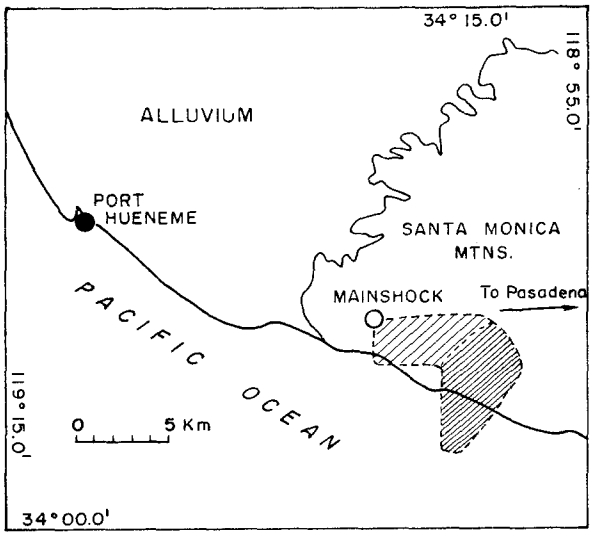

FIG. 1. Location map, showing strong-motion instrument site, mainshock, and aftershock locations. The azimuth to Pasadena is also indicated. The aftershock locations are shown by the shaded areas. The dense shading corresponds to most of the aftershocks, especially with magnitudes greater than 2. A few aftershocks of magnitude 0 to 2 were located in the lightly shaded region, and several large aftershocks occurred near the main-shock focus.

converted waves, and surface waves are of little importance. Recordings of the earthquake at distant stations may be significantly influenced by these effects. We cannot, however, ignore the effect of geological heterogeneities on the Port Hueneme record. Port Hueneme is situated on a thick section of sediments, while the earthquake probably took place in crystalline basement. We have made some simple calculations of the effect of the sediments on the waves and find that the surface record can be compensated for the sediments by decreasing the amplitude of the motion and compressing the time scale.

The earthquake was recorded at Port Hueneme on U.S. Coast and Geodetic Survey (USCGS) standard type accelerographs and on Carder Displacement Meters (CDM). The accelerograms and CDM records are displayed in Figure 2 (after digitization from blueline copies of the original record). The published orientation of the components is within 5° of the actual orientation (Maley, personal communication, 1975). The most striking motion occurs on the NS component. It is the *S*-wave energy in this component that we will attempt to model. The EW motions are too sensitive to uncertainties in the *S*-wave radiation pattern, and the vertical motion is so small that there is nothing to

model, although this tells us that the S waves have been refracted toward vertical incidence near the station. For a number of reasons, discussed in Boore and Zoback (1974), we prefer to model the velocity records. These are shown in Figure 3. The integration scheme used to obtain the velocity records employs a low-cut filter to diminish long-period uncertainties in the base line. It made little difference on the velocity wave forms whether the long-period roll-off started at 0, 0.2, or 0.4 Hz. Therefore, we feel that the velocity wave forms are a good representation of the true ground velocity at Port Hueneme. For completeness, the displacement records are shown in Figure 4. A low-cut filter with a cosine taper between 0.1 and 0.2 Hz was used. From here on we will refer to the velocity records only in our discussion.

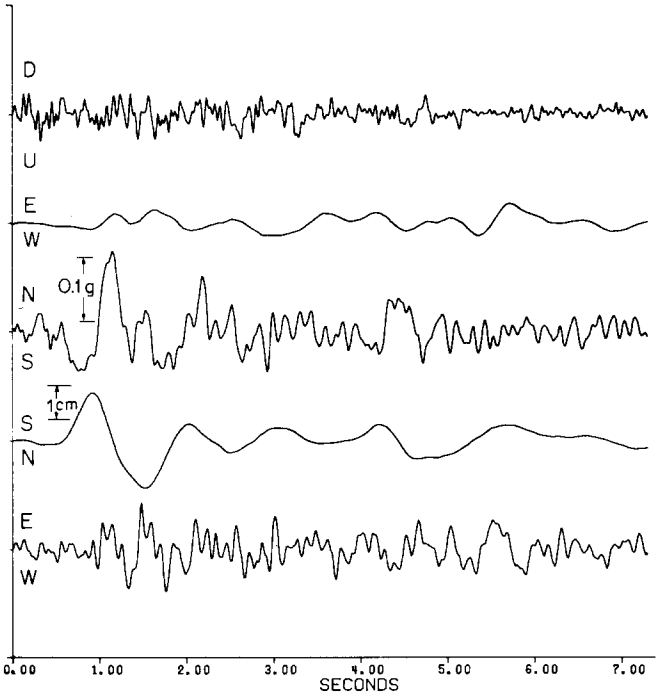

FIG. 2. The accelerometer and CDM data as recorded (after digitization and plotting in original format). The 1-cm scale shown for the NS CDM refers to the distance on the record, not to the ground motion.

The phase beginning at A in Figure 3 is presumably the initial S wave from the earthquake. Since the initial P wave should be about 3 sec earlier, the instrument must have triggered about 2.5 sec after the arrival of the first P wave. Late triggering is common in instruments with horizontal starters. The S arrival on the EW component would be picked at B, well after the obvious arrival on the NS component. As shown below, the S motion on the EW component is sensitive to the local azimuth of approach of the waves. The apparent shift in the S arrivals on the two horizontal components may be a result of the propagation of the fault rupture to the south and the resulting change in the azimuth from the station to the point of energy radiation.

The horizontal components were combined into particle velocity-motion plots (Figure 5). Although these plots do not show the ground displacement directly, they are useful for studying phase arrivals and polarization angles. The section from A to B represents a southward motion inclined at about 5° clockwise from due south. At B the motion

reverses and, with the addition of more motion on the EW component, the orientation changes to about 13° clockwise from due north. The phase starting at about 1.3 sec in Figure 3, with the trough marked by C, probably corresponds to a separate arrival either from a wave travelling along a non-least-time path, or from a separate earthquake initiated by the main shock, but with a different focal mechanism. The evidence that this is a

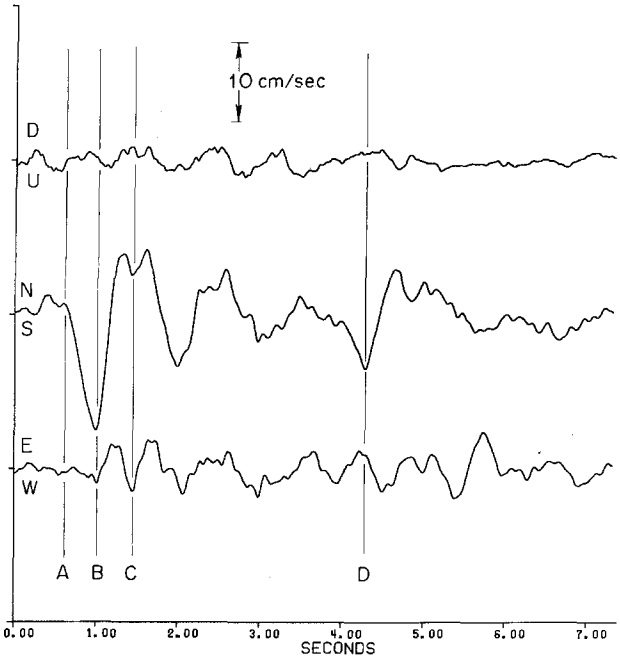

FIG. 3. Velocity traces.

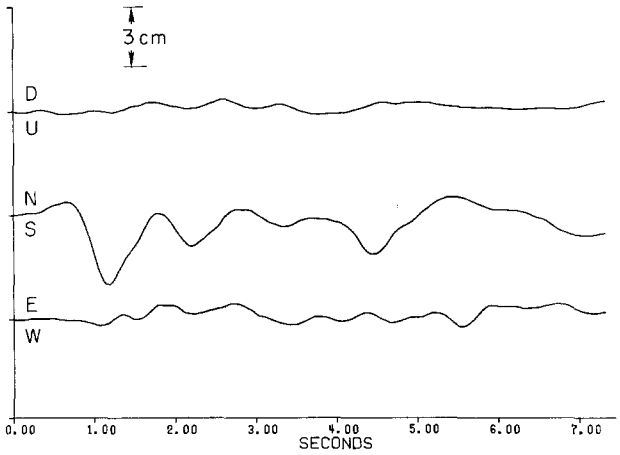

FIG. 4. Displacement traces.

separate arrival is clearly revealed in the particle motion plot, where the motion is seen to be rectilinear with an orientation completely different from the initial motions. Based on this evidence, we can ignore this phase in our attempts to model the motion from the main shock. In the later part of the velocity traces, the orientation of the particle motion changes considerably. This change is first noticeable at about 4 sec and corresponds to the phase whose trough is marked by D in Figure 3. These later motions could be due

to reverberations in the sediments beneath Port Hueneme or to extensions of the initial main-shock rupture or aftershocks with focal mechanisms different than that of the main shock. Considering the complexity of these later motions, we have ignored them in our model fitting, concentrating instead on the first half-cycle of motion between points A and C.

In modeling the motions produced by faults it is desirable to constrain as many parameters as possible. For the Pt. Mugu earthquake the fault-plane solution obtained, taken at face value, puts strong constraints on the orientation of the fault plane and the

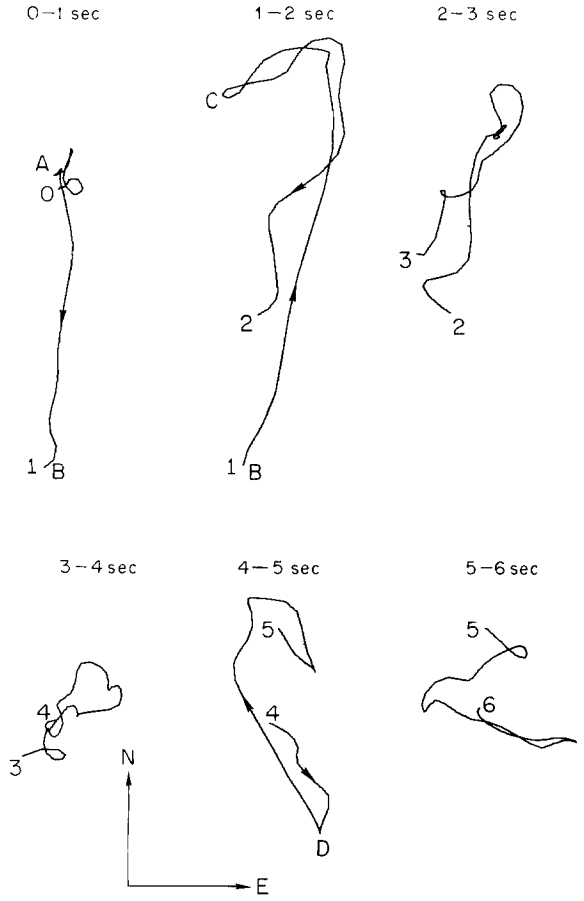

FIG. 5. Particle velocity diagrams for 1-sec windows.

direction of initial slip (Figure 6). The crustal model derived by Stierman and Ellsworth (1976) was used to compute the takeoff angles used in plotting the initial motions. The geology in the region, with the north dipping Malibu coast and Santa Monica faults (Campbell, personal communication, 1975) would argue that the north dipping plane in Figure 6 is the fault plane. The seismological evidence for this is somewhat inconclusive. The aftershocks, which are usually the prime evidence for determining the fault, are not distributed along a well-defined plane (Stierman and Ellsworth, 1976). We have assumed the north dipping plane in the modeling that follows, although the choice is not critical to our general conclusions.

The consistency of the *P*-wave fault-plane solution and the observed *S*-wave motion at Port Hueneme has been checked by computing theoretical *S*-wave polarization angles

from formulas of Hirasawa (1970). The theoretical results, expressed as clockwise angles from the north, are shown in Figure 7 for a range of takeoff angles at the source and a range of azimuths from the event to the station. The *top* figure assumes the local angle of incidence is given by the complement of the takeoff angle (i.e., straight-line propagation). The *bottom* figure assumes that refraction toward the vertical has produced a nearly vertical angle of incidence near the station. The lack of motion on the vertical component in Figure 3 would agree with this. The values corresponding to the takeoff angle (137°) and azimuth (289°) given by a straight-line path from Stierman and Ellsworth's (1976) hypocenter to the Port Hueneme station are shown by circled x's. Because of refraction toward the vertical, the actual takeoff angle is probably less than 137°. The observed polarization angles (from points A to B and beyond point B in Figure 5) are shown by dashed horizontal lines.

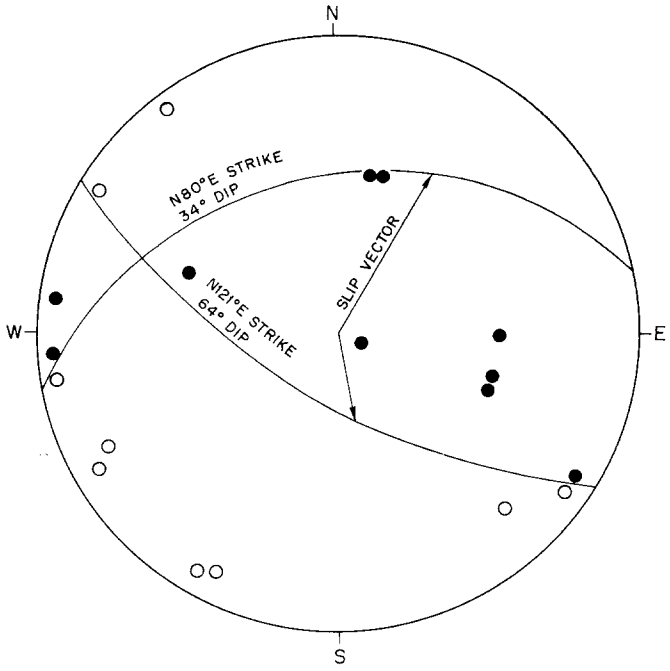

FIG. 6. First-motion data (● compression, ○ dilatation) and fault-plane solution.

The observed and theoretical polarization angles do not agree, by as much as 30° to 40° if the azimuth of 289° is correct and the angle of incidence is close to vertical near the station. There are a number of reasonable explanations for this. The orientation of the fault plane may be off by 10° or so, $P-SV$ coupling may distort the S-wave polarization (e.g., Gutenberg, 1952), and lateral refraction in the complicated geology may produce a local propagation direction different from the azimuth to the epicenter. If the geology produced a lateral refraction to the north, the apparent azimuth would increase and from Figure 7 we see that this would help explain the difference between the theoretical and observed polarization angles. We studied this last possibility by calculating the horizontal deviation of propagation produced by refraction across a plane whose strike was not normal to the propagation direction (Figure 8). The results show that significant lateral refraction can reasonably be expected if the strike of the geology is close to the propagation direction. This is the case, since the predominant strike of the structure in this part of the Transverse Ranges is west or slightly southwest. We feel that the combination of

variability in the fault plane solution and the strong possibility of lateral refraction can account for the difference between the observations and theory. Note that because the motions are small, the variations show up most strongly on the EW component (the polarity of the EW motion changes with a 10° or less change in azimuth). Thus in the

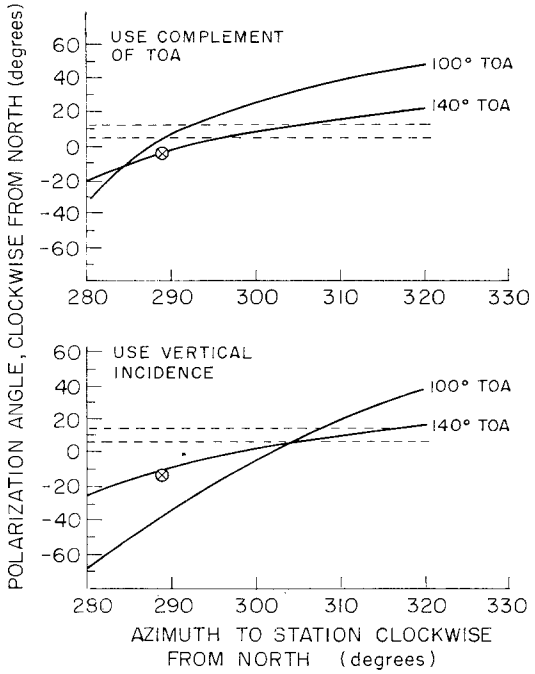

FIG. 7. Polarization angles, clockwise from north. The observed angles are shown by the dashed lines. The theoretical angles have been computed for a range of azimuths and takeoff angles (TOA). ⊗ represents the azimuth and TOA given by the straight line between the hypocenter and Port Hueneme. The *upper* graph has used the straight-line path assumption in computing the polarization angle. The *lower* graph assumed that the rays are refracted to the vertical beneath Port Hueneme. Note that the polarity of the EW component is sensitive to the azimuth of approach.

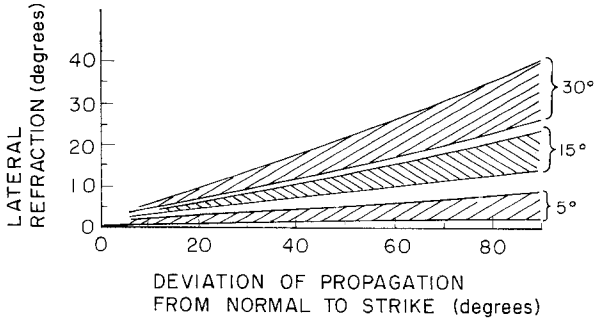

FIG. 8. Lateral refraction for a range of dips (5° to 30°) and velocity contrasts (β_1/β_2 = 1.5/2.0 for the lower boundary of each envelope and β_1/β_2 = 1.0/2.0 for the upper boundary). The incident ray had a 45° angle of incidence with respect to the vertical.

modeling we will concentrate on the NS component of the velocity trace, which shows the dominant motion. Because of the uncertain azimuth to the source, we have not rotated into *SH* and *SV* components.

The effect of local geology can produce not only lateral refraction, but also first-order effects on the amplitude of the ground motion. The Port Hueneme station rests on a thick

section of sedimentary rocks. Oil wells in the vicinity show Eocene sediments at depths of 3.6 km (Dosch and Mitchell, 1964). Well logs and velocities in similar rocks elsewhere were used to construct a possible shear-wave velocity depth-section (Table 1). A wave form similar to the observed velocity pulse was propagated through this section using the method of Joyner and Chen (1975), which takes into account nonlinear soil behavior. The nonlinearity is not expected to be important. Vertical incidence at the base of the sedimentary column is assumed. This is not a critical assumption, for an incidence of 50° from the vertical will reduce the surface motions by about only 10 per cent (assuming *SH* waves only). The input and surface motions are shown in Figure 9. The input motion is

TABLE 1
SOIL PROFILE

Layer-Thickness (km)	Shear Velocity (km/sec)	Density (gm/cc)
0.5	0.22 → 0.55	2.05
0.8	0.85	2.20
3.7	1.70	2.40
—	3.40	2.70

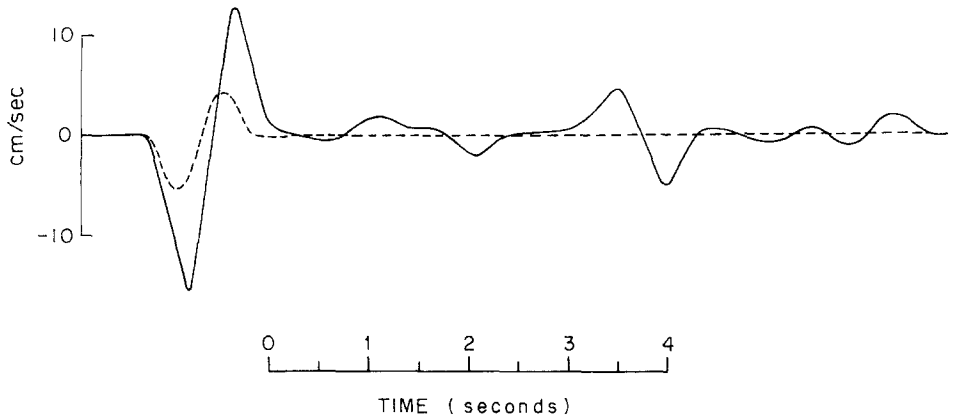

FIG. 9. Results of the sedimentary layer calculation. The dashed curve is the input motion that produces the surface motion (shown by the solid curve). The amplitudes are directly comparable, for the dashed curve represents the motion that would be recorded at the free surface in the absence of a column of soils and sedimentary rocks.

the same as the surface motion that would be recorded in the absence of a soil section. For practical purposes, the surface motion is simply a scaled version of the input motion. The next obvious phase, at about 5 sec after the first *S* wave, is due to a multiple reflection off the interface at 1.4 km in the model. This suggests that the later phase seen in the observed data (marked *D* in Figure 3) may be due to local geology rather than to the source. The difference in particle motion between this phase and the initial phase, however, indicates that if it is a result of geology, the layer from which the later phase is reflected is not flat laying (compare the plots for 0 to 1 sec and 4 to 5 sec in Figure 5).

Since in the next section we match the observed motion to synthetics in which a homogeneous perfectly elastic material is assumed, we checked the effect of Q attenuation in propagation from the hypocenter to the base of the sedimentary section. Application of a Q operator (Carpenter, 1966) with $Q = 300$ showed that the main change to the input

pulse in propagation over 24 km was a reduction in peak amplitude of about 7 per cent. The wave form did not change shape.

In summary, on the basis of the soil response and particle motion studies, the data that we will attempt to model have been reduced to a scaled-down version of the first $\frac{1}{2}$ to 1 cycle of the S wave on the NS component. The amplitude of the motion, after compensating for the soil response by a factor of 2.8 and for the free surface by a factor of 2.0 is 2.7 cm/sec. The time scale has been reduced by a factor of about 0.9. The assumed whole-space amplitude of 2.7 cm/sec is probably a lower limit. Compensation for Q and the nonvertical angle of incidence may increase this number by up to 20 per cent; the last four columns in Table 2 would be increased proportionately.

Models

Several different models of the rupture propagation were used to deduce source properties from matches between observed data and synthetic seismograms. The models include the Brune (1970), Haskell strip source (Haskell, 1964; Savage, 1972), Haskell extended source (Haskell, 1969), and Savage (1966) models. These models all have the common assumption that the faulting takes place in a uniform, homogeneous, infinite medium. In the previous section we compensated the observed motion for the soil layers; this gave a reduction factor in amplitude of about 2.8. To compensate for the free surface, we used a reduction factor of 2. This factor is exact for SH motion, which is prominent in the Pt. Mugu record, and is not a bad assumption for steeply incident SV waves (Anderson, 1975). Thus the observed surface motion, with a peak amplitude of 15.1 cm/sec, has been scaled down to 2.7 cm/sec in order to approximate the infinite space record which can then be compared with the synthetic seismograms.

With two exceptions (clearly labeled) all of the synthetic seismograms have been computed for rupture on a plane with a 34° dip in the N10°W direction. The relative slip vector has 0.8 parts of reverse slip and 0.6 parts of left-lateral strike slip. The shear velocity is 3.43 km/sec (Stierman and Ellsworth, 1976) and the assumed rupture velocity of 3.1 km/sec was chosen as 0.9 of the shear-wave velocity. The rupture velocity is not constrained in our study, and we have used 0.9 β for convenience. The size of the implied source parameters is inversely proportional to the rupture velocity. The rigidity has been taken as 3×10^{11} dynes/cm^2.

The Brune model predicts the shape of the far-field displacement and velocity pulses as

$$u = \{\mathrm{RAD}\} \frac{7\pi}{16} \frac{D\beta}{r} t \exp(-2.34\beta t/R) \tag{1}$$

$$\dot{u} = \{\mathrm{RAD}\} \frac{7\pi}{16} \frac{D\beta}{r} \left(1 - \frac{2.34\beta}{R} t\right) \exp(-2.34\beta t/R) \tag{2}$$

where $\{\mathrm{RAD}\}$ = radiation pattern, D = average dislocation on the fault surface, β = shear velocity, r = hypocentral distance, R = radius of the fault, and t = time after arrival of the first motion. By roughly fitting these forms to the data (fitting peak motions and the time of either the zero crossing in the case of velocity, or the pulse width in the case of displacement) we find the fault parameters listed in Table 2. In doing the calculations, $\{\mathrm{RAD}\} \cong 0.5$ for the fault-station geometry present.

Although simple, and apparently quite successful for studies in which large amounts of data are available over a range of azimuths (e.g., Thatcher and Hanks, 1973), the Brune model assumes instantaneous rupture over the fault surface and thus seems of limited use for detailed studies of seismograms recorded close to faults. The remaining models

TABLE 2
MODEL AND FAULT PARAMETERS*

Model	Radius (km)	Rise time (sec)	D (cm)	$M_o(10^{24}$ dynes/cm)	$\Delta\sigma$ (bars)	σ_e (bars)
Brune						
displacement	1.6	—	92	2.2	240	—
velocity	4.0	—	26	3.9	30	—
Figure 10						
strip	1.66, 2.5†	0.25	135	1.2	260	480
extended	1.66, 2.5	0.25	270	2.5	520	960
Figure 11						
(1)	2.8	0.30	43	3.2	60	130
(2)	2.8	7.7‡	50	3.7	70	220
(3)	2.8	3.8‡	67	4.9	100	150
Figure 12						
(1)	1.6	0.38	72	1.7	190	170
(2)	2.2	0.34	48	2.2	90	130
(3)	2.8	0.30	43	3.2	60	130
(4)	3.9, 2.5§	0.30	50	4.6	70	150
Figure 15						
(1)	4.5	0.34	18	3.5	20	50
Figure 16						
$V = 1.6$	0.58	0.38	514	1.6	3650	1890
$V = 3.1$	1.6	0.38	72	1.7	190	170

* The rise time refers to a finite ramp except for Figure 11, (2) and (3), which correspond to a source function $1-\exp(-\gamma t)$. $\bar{D}$ is the average dislocation over the fault surface, taken as two-thirds the peak dislocation. M_o is the seismic moment, given by $M_o = \mu\pi R^2\bar{D}$ where $\mu = 3\times10^{11}$ dyne/cm^2 and R = radius. $\Delta\sigma$ = stress drop over the fault surface and is given by $\Delta\sigma = (7\pi/16)\mu\bar{D}/R$, except for the Figure 10 models, in which case $\Delta\sigma = 1.06\,\mu\bar{D}/FL$, where FL = fault length (Chinnery, 1969). σ_e = effective stress and is given by $\sigma_e = (\mu/\beta)(1+\beta/V)\bar{U}$ (Kanamori, 1972) where $\bar{U}$ = effective dislocation velocity on one side of the fault. $\bar{U} = 0.5\,\bar{D}/RT$, where RT is the rise time, for finite-ramp source functions, and $\bar{U} = 0.32\,\gamma\,\bar{D}$ for exponential source functions, where $\bar{U}$ has been averaged over a time $t = 1/\gamma$ (Kanamori, 1972).

† Fault length, fault width.

‡ γ of exponential rise (see footnote to title).

§ Semimajor, semiminor axes.

discussed in this paper have in common finite rupture propagation. It is easy to show that rupture propagation can have a profound influence on the wave forms. For example, the far-field velocity wave form for S motion from the Haskell strip dislocation is given by

$$\dot{u} = \frac{\mu\{\mathrm{RAD}\}}{4\pi\rho\beta^3}\frac{A}{r}\left[\frac{\dot{D}(t-t_E)-\dot{D}(t-t_B)}{t_E-t_B}\right] \tag{3}$$

(Savage, 1972) for unilateral rupture where A = area of faulting, $\dot{D}$ = velocity of total dislocation on fault surface and t_B, t_E are the times at which energy arrives from the beginning and end points of rupture; these times depend on rupture velocity. The strip model is so named because the length of the fault is assumed to be longer than the width; furthermore, integration over the width, W, is approximated by simply multiplying by W.

We can write the maximum displacement predicted by the Haskell model as

$$u_{\max} = 0.08\,[\beta/V-\cos\theta]^{-1}\,[AW/L]^{1/2}(D/r)\{\mathrm{RAD}\} \tag{4}$$

where θ = angle between the line of rupture and the line from the origin of rupture to the observation point, V is the rupture velocity, and W = the width of the fault. For comparison, the Brune equation (1) gives

$$u_{\max} = [0.12][A]^{1/2}(D/r)\{\mathrm{RAD}\}. \tag{5}$$

If we assume $L = 10\ W$ and $V/\beta = 0.9$, we find that equation (5) is larger than equation (4) for all angles θ greater than 26°. Thus if rupture velocity is taken into account, the inferred dislocation, D, can be quite different from that estimated by the Brune model. In both cases, however, the area under the displacement pulses, and consequently the moment, is the same for both models.

The simple Haskell wave form in equation (3) can be very useful in making rough approximations to fitting the observed data. For example, Figure 10 shows the wave form predicted for a finite-ramp dislocation function. The overall features are similar to the observed data, with an initial negative lobe, followed by a positive swing; the time separation of the pulses and their widths, and the amplitudes can be used to estimate the fault parameters. As is clear from equation (4), the results will depend on the direction of rupture. If the rupture is toward the NE along the fault plane striking N80°E (Figure 6), the fault length must be very short (less than 1 km) if $t_E - t_B$ is to be on the order of 0.4 sec, the time separation between peaks on the observed data. On the other hand, if the rupture has a component toward Port Hueneme, the length of rupture must be close to 3 km. If the rupture is bilateral, the most important part as far as the intial half-cycle of motion is concerned is the part rupturing with a component in the direction of Port Hueneme. The same value of 3 km is found for the fault length. These estimates assume $V/\beta = 0.9$; smaller values require smaller fault lengths.

From these simple considerations, we can say that the rupture contributing to the first $\frac{1}{2}$ cycle or so of the Port Hueneme velocity trace must be a fault of short length. The distribution of main-shock and aftershock epicenters (Figure 1) suggests that the rupture propagated unilaterally toward the SE. Our modeling shows that if this is true, the first coherent rupture must have gone an extremely short distance (about 1 km), not nearly as far as suggested by the aftershock distribution. Furthermore, if rupture was unilateral toward the east, amplitude considerations require dislocations about three times larger than if the rupture had a significant extent toward the Port Hueneme station.

Although the time relations given by the Haskell strip model are useful, the detailed wave forms and inferred fault parameters are open to question. Figure 10 shows the velocity wave form computed from equation (3) for the parameters given in the caption. The parameters estimated from this wave form are given in Table 2. The rupture was updip, giving a fault length intermediate between those obtained with rupture toward and away from the station. The width is a free parameter and was arbitrarily taken to be somewhat larger than the length, in violation of the assumption of the Haskell strip model that the length is greater than the width. On the other hand, if we had taken, for example, $L = 10W$, the implied dislocation would have been close to 2000 cm. Furthermore, the block-like shape of the computed pulses is obviously a poor fit to the observed wave form. For these reasons, the simple Haskell strip model is too simple for detailed modeling, although the predicted time relations can be used to give information about fault length. We can make an improvement of the strip model by realizing that the contributions from each strip will not arrive simultaneously, even if rupture is assumed to occur instantaneously along the width (Haskell, 1969; Boatwright and Boore, 1975). The effect will be to smooth out the box-like wave forms. The smooth curve in Figure 10 was computed in this manner for the same fault parameters that produced the box-like wave form. This smoothing implies that the ω^{-2} high-frequency decay often attri-

buted to the Haskell source model (e.g. Savage, 1972) will more likely be ω^{-3} if the finite width of faulting is taken into account, even with instantaneous rupture over the width.

The fault parameters deduced from the smooth curve in Figure 10, which is a reasonable first-order fit to the data, are very large (270 cm dislocation, stress drop close to 500 bars). These numbers might be reduced if other directions of rupture were assumed, but the instantaneous faulting along an edge is such an undesirable feature that this model was dropped. While the general Haskell (1969) formulation is applicable to any space-time history of rupture, it is cumbersome to recast the commonly used strip formalism (Boatwright and Boore, 1975) to a more realistic model of faulting. We turn to a dislocation model proposed by Savage (1966) in which rupture initiates at a point and spreads circularly until it intersects a boundary curve, where it stops. The boundary, which can have any shape, is elliptical in our models. The slip can initiate at any point within the

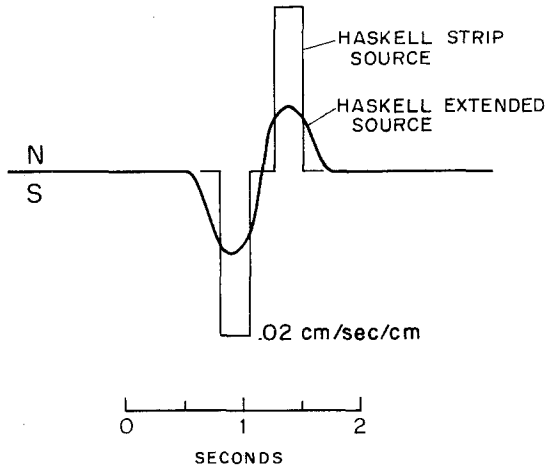

FIG. 10. Theoretical wave forms at Port Hueneme for the same rectangular fault model, using the Haskell strip source in which the integration over the width of the rectangle (2.5 km) is carried out by simply multiplying by the width, and using the Haskell extended source in which a true numerical integration is carried out over the width. The fault propagation was unilateral, updip in the S10°E direction at a rupture velocity of 3.33 km/sec, over a fault length of 1.7 km. The rise time of the finite ramp source was 0.25 sec. The number 0.02 cm/sec/cm is the velocity given by 1 cm of fault dislocation, not accounting for the free surface.

ellipse and propagates at a constant velocity. The amplitude of the slip varies elliptically over the rupture surface. The function describing the variation of the slip at any point with time is assumed to be independent of position on the fault surface. This model of faulting is very easy to program and seems quite useful (e.g., Filson, 1975). The computations are valid, however, only if the far-field terms dominate and if the fault dimensions are small enough to justify an expansion of the distance between a local point of rupture on the fault surface and the observation point in a Taylor series, keeping only first-order terms. The far-field assumption is satisfied since Port Hueneme is at least five wavelengths from the focal region. The first-order Taylor series expansion is valid if $F/r \ll 1$, where F = largest fault dimension, and r = hypocentral distance. For our case $F \cong 3$ to 8 km, $r = 24$ km, so $F/r = \frac{1}{6}$ to $\frac{1}{3}$, which is sufficiently small.

Two source-time functions were used: a finite ramp and an exponential ramp. The motion from a ramp of 0.3 sec rise time is shown in Figure 11 for one model of the earthquake. For comparison, the motions for two exponential ramps are also shown. As might be expected, the wave forms produced by the exponential ramp are smoother than those

produced by the finite ramp. The source functions, scaled to the inferred dislocation amplitudes, are compared in the *bottom* of Figure 11. The inferred fault parameters are given in Table 2. Although the overall wave shapes can be made comparable by a choice of γ between 3.8 and 7.7, the fault parameters estimated from the exponential source function for this model will be consistently larger than the parameters estimated from the finite ramp. This is an example of the nonuniqueness which can occur in source studies. For simplicity a finite ramp source function is assumed for the rest of the wave forms shown in this paper.

Based on the relative locations of the main-shock and aftershock locations, our initial efforts at fitting the Port Hueneme record involved unilateral rupture along the fault plane in directions away from the station. Large dislocations (on the order of 5 to 10 meters) were required to fit the observed record. Furthermore, difficulty was encountered in matching the slope of the initial downbreak; the synthetics gave slopes which were too steep.

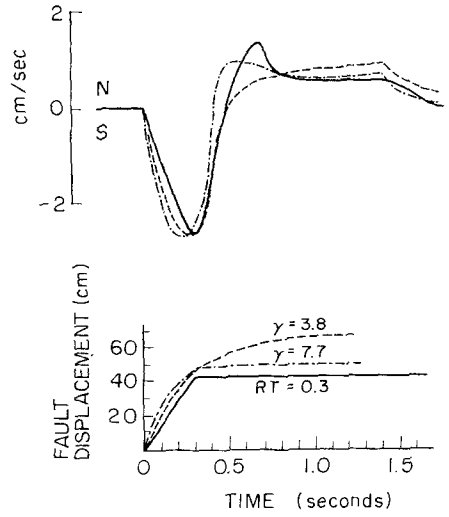

FIG. 11. Theoretical infinite space wave forms at Port Hueneme for a circularly spreading dislocation initiated at the center of a 2.8-km radius circle. The wave forms are shown for three different source-time functions (*bottom*). The exponential functions have the form $1-\exp(-\gamma t)$.

From the study of the Haskell strip model, we realized that a much better fit could be achieved by propagating the rupture in the general direction of the station. We show a series of models in Figure 12, all of which have about the same distance between the focal point of rupture and the boundary closest to Port Hueneme. With minor adjustments of the rise time and fault geometry, all of the models are an equally good fit to the first half-cycle of the observed velocity trace. In other words, the first part of the *S* wave observed at Port Hueneme contains little information about the progress of rupture away from the station.

As shown by the theoretical curves in Figure 12, the second half-cycle (the positive lobe and beyond) provides information on the rupture away from the source. It would seem possible to rule out model 4, which comes the closest to filling the gap between the hypocenter and the aftershock locations, on the basis of the long duration of positive velocity. On the other hand, the observed seismogram has a pronounced negative motion following the first cycle. There is no way that the theoretical models can produce this motion if the faulting is characterized by monotonic slip on a single surface. The easiest

way of explaining this subsequent motion is to postulate a second "earthquake", delayed in time and perhaps shifted in space (toward the aftershocks). For example, Figure 13 shows the result if the wave form of the second event is taken to be a delayed and attenuated version of the wave form of model 2 (Figure 12). The comparison with the data is very good. A deacceleration and acceleration of the rupture or a zone of reduced slip [such as found for the 1971 San Fernando earthquake (Alewine, 1974)] would produce the required motions. Because of this possibility, we cannot rule out model 4 since subsequent rupture might eliminate the long, positive tail in the velocity wave form.

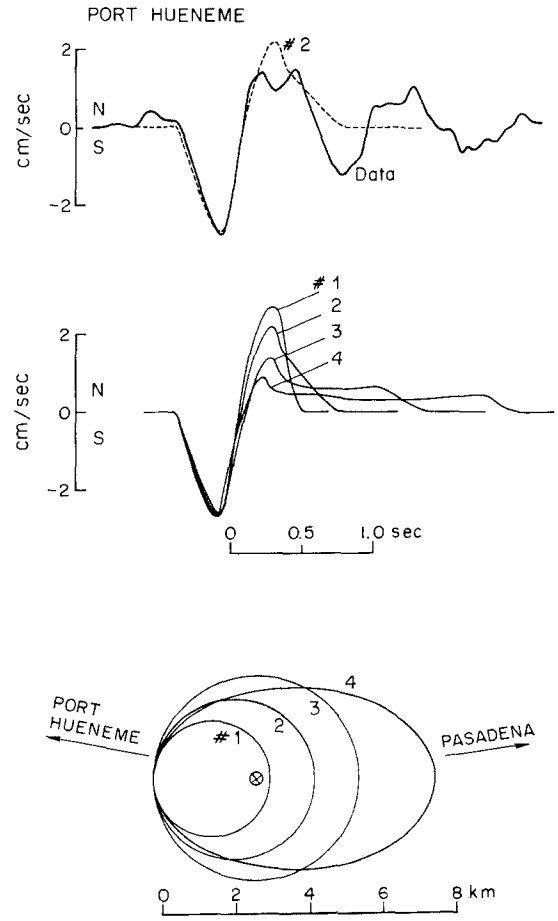

FIG. 12. Theoretical infinite wave forms at Port Hueneme for rupture starting at the circled x and stopping when the four curves shown at the *bottom* are encountered. See Table 2 for dimensions and rise times. The *top* of the figure shows a comparison of model 2 (dashed) and the data. Note that none of the theoretical models have a second downswing. The later motion in the data may represent a second "earthquake" (see the text).

Some constraints on the initial rupture away from Port Hueneme can be given by strong-motion recordings to the east of the focal region. Fortunately a good record was obtained on a low magnification (4×) intermediate period (10 sec) seismograph (Kanamori, personal communication, 1975). The theoretical models of Figure 12 are compared with the NS component at Pasadena (which contains almost pure *SH* waves, uncontaminated by $P-SV$ coupling) in Figure 14. Model 2 gives the best fit. No compensation has been made for effects of soil layering near Pasadena. If the soils amplify the waves (Gutenberg, 1957), we should be comparing the theoretical motion in Figure 14 with a

reduced version of the observed motion. Model 1 would then be a possible fit. At any rate, the models with well over half the rupture surface away from Port Hueneme are clearly rejected.

Up to this point we have assumed, mainly on geological grounds, that the faulting took

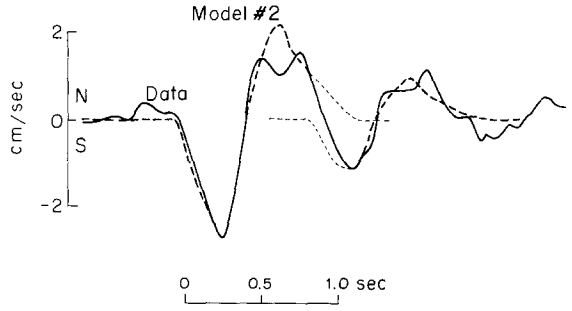

FIG. 13. Theoretical wave form (heavy dashed line) resulting from delay and sum of wave forms in model 2 (light dashed lines), compared with data (solid line). This shows that a multiple earthquake is consistent with the data.

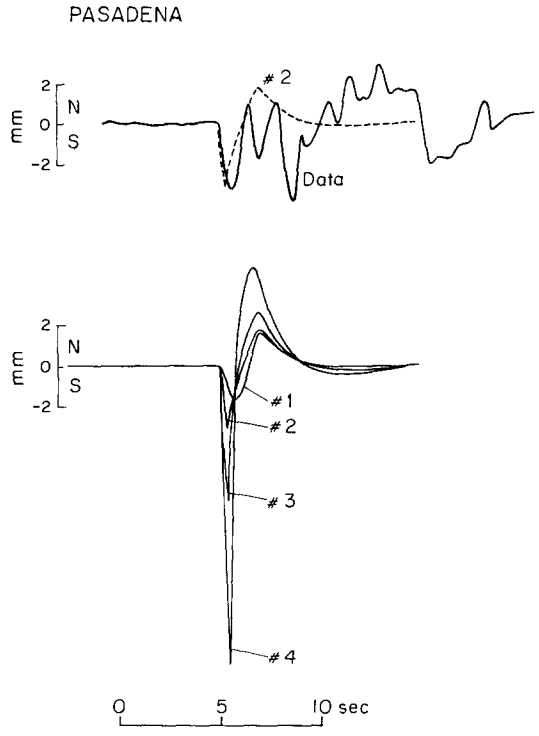

FIG. 14. Theoretical wave forms at Pasadena as recorded on a long-period (10-sec) pendulum of low gain (4×) for the four models of Figure 12. The motions have been doubled to approximate the free surface. No attenuation has been included in the propagation. Attenuation would round off the corners and reduce the overall amplitude of the theoretical traces by about 20 per cent. Local soil amplification, which has not been included, would help offset the attenuation.

place on the plane striking N80°E (Figure 6). There is a possibility from the orientation of the aftershock locations, however, that the rupture occurred on the auxiliary plane striking N 121°E (see Figure 7 in Stierman and Ellsworth, 1976). We devised a fault model (Figure 15) which would fit the Port Hueneme record as well as the previous models; but

this model gave a very poor fit to the Pasadena record. Although a better fit is undoubtedly possible, with appropriate parameter adjustments, we have not pursued a model of rupture on this plane. Our strongest conclusions are not dependent on which fault plane is assumed to rupture.

Our hypothesis that the rupture was a multiple event is based primarily on the Port Hueneme data and the fit between theory and observation shown in Figure 13. It is possible, of course, to fit almost any complicated wave form by appropriate combinations of simpler wave forms, and thus the comparison shown in Figure 13 is not a conclusive test of our hypothesis. It is natural to suspect that the extra wiggles in the data are due to reverberations due to geological heterogeneities. This is unlikely in our case. First, the particle motion plots of Figure 5 show that the later motion of concern, between 1.5 and 3.0 sec, has particle motions similar to the initial *S* arrival and thus has not been

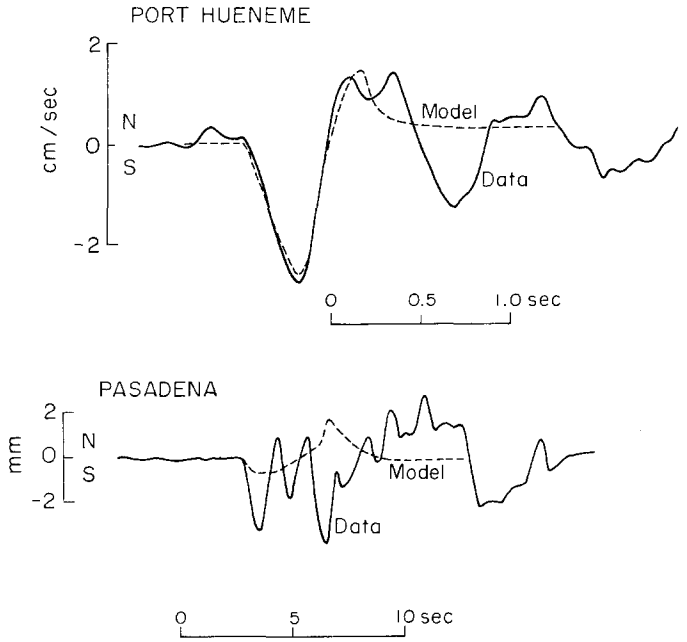

FIG. 15. Theoretical wave form at Port Hueneme and Pasadena for rupture in the fault plane striking N121°E. The rupture started 3.4 km from the center of a circle of 4.5 km radius (with the long direction of rupture toward Port Hueneme). The fault geometry was chosen to produce a wave form at Port Hueneme similar to those in Figure 12.

strongly refracted, as might be expected if geological reverberations due to complicated geology were the cause of the later motion. Second, the simulation of the response of the local geology beneath Port Hueneme shows that although the velocity of the sediments decreases rapidly toward the surface, there are no strong second arrivals in the time window of interest. This is because we have modeled the near-surface velocity structure as a continuous transition. If the later motion were due to a reverberation, the large amplitude would require a sharp impedance contrast of about 3 to 1, and the delay requires that this contrast be in the upper 200 meters (assuming that the reverberation is from the surface to an interface and back). We see no evidence from the geological information available to us of such a sharp contrast in material properties over depth scales of sufficient extent to produce a strong reverberation.

If a second earthquake did occur, and if it was toward the aftershock concentration,

then the delay at Pasadena between the *S* waves from the first and second events can be estimated to be less than 0.5 sec. Thus the additional later oscillations of the Pasadena record (Figure 14) cannot be used as evidence for the second earthquake. These later motions may be due to the crustal layering. For example, according to the crustal model used by Stierman and Ellsworth (1976) the direct *S* wave at Pasadena from a source at 17-km depth should be followed about 1 sec later by a head wave and a wide angle reflection from the Mohorovičić discontinuity. Simulations of the motions from a *SH* line source show that the generalized reflection will be very similar in shape to the direct wave and somewhat smaller in amplitude and in particular would have the proper phase to account for at least the second swing to the south in the Pasadena record (Figure 14). Unfortunately, the *S*-wave radiation pattern computed from the fault plane solution of Figure 6 shows that the reflected motions leave the source very close to a node. Thus although the time relation and phase are adequate to explain at least one of the extra oscillations in the Pasadena record, it is difficult to account for the amplitude of these later motions.

Discussion

The fault parameters inferred from the different models discussed thus far are summarized in Table 2. The dislocation averaged over the fault surface is less than 1 m and the average stress drop and the effective stress are on the order of 50 to 200 bars. These numbers are greater than estimated by both the Brune (1970) model and by the preliminary analysis reported by Ellsworth *et al.* (1973). The estimated parameters are considerably less than estimated from the Haskell models of Figure 10, which give stresses ranging from 250 to 1000 bars. The main reason for this difference is that the direction of rupture in these models was not toward Port Hueneme, and thus there was little of the focusing of the radiated energy which played such an important part in the models in which rupture initiated at a point.

The seismic moments are fairly consistent between models. Model 2 of Figure 12, which gave the best fit to both the Pasadena and Port Hueneme records, gives a moment of about 2×10^{24} dyne-cm. Considering both that the size of the zone roughly outlined by the aftershocks is considerably larger than the area of model 2, and that a second earthquake may have helped make up the difference in areas, a moment near 2×10^{24} dyne-cm is probably a lower bound. The values of moment determined in Table 2 are consistent with the data of Thatcher and Hanks (1973) for many southern California earthquakes. (Using their moment-magnitude-radius relation implies $M_L = 6.0$ for the parameters of model 2; this is the magnitude assigned to the earthquake.)

Unfortunately, the nonuniqueness in all estimated fault parameters except the moment may be worse than indicated so far. We have assumed a rupture velocity of 3.1 km/sec. We could obtain similar wave forms with combinations of rupture velocity and fault dimensions which preserved the time differences between initiation and stopping of the rupture. As an example, Figure 16 shows a comparison of the model 1 wave form (Figure 12) with that computed for a rupture propagating at half the velocity (1.55 km/sec). The Port Hueneme seismograms are virtually identical. The moment from the slower rupture is comparable to those found earlier, but very large fault dislocation and stresses are required on a fault of small area (Table 2). Although we may reject this model on account of the extreme parameters required, it is not clear where to draw the line. Independent estimates of rupture velocity from theoretical work give terminal velocities ranging from close to the shear-wave velocity (e.g. Kostrov, 1966) to the compressional-wave velocity (Burridge and Levy, 1974). Furthermore, recent work indicates that the

terminal velocity may not be attained, depending on the details of the fault geometry and strength (Husseini *et al.*, 1975). In general, the size of the derived source parameters bears an inverse relationship to rupture velocity.

Although we make no claims to uniqueness for our estimates of the fault parameters, we do believe that a number of general conclusions can be reached.

1. The rupture producing the first part of the *S* wave was bilateral. The portion of rupture away from the aftershock locations was of prime importance in determining the initial motions at Port Hueneme.

2. Although the rupture also propagated away from Port Hueneme, the motions at Pasadena can be used to argue that the initial coherent phase of the rupture did not fill in the region outlined by the aftershocks. This is in agreement with the results of Ellsworth *et al.* (1973). It is quite likely, however, that a second rupture followed the first; this second rupture (and possible subsequent ruptures) may have extended out to the aftershock zone.

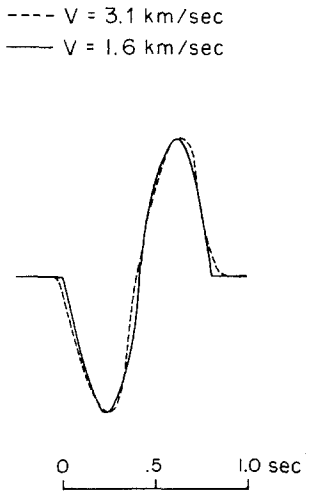

FIG. 16. Theoretical wave forms at Port Hueneme for model 1 of Figure 12 (dashed) and for the same model but with a slower rupture velocity and correspondingly smaller fault dimensions (solid). With the exception of the seismic moment, the inferred fault parameters are grossly different (see Table 2).

3. A lower bound to the seismic moment may be 1.5×10^{24} dyne-cm. The total moment released in the rupture process may have been as much as 5×10^{24} dyne-cm. The inferred stress drops are variable, but are in the range of 50 to 200 bars. The fault parameters we infer are generally larger than those found by Ellsworth *et al.* (1973), but are not large enough to account for the vertical leveling data discussed by Castle *et al.* (1976). The inconsistency in the moments required by the static vertical leveling data and the dynamic strong-motion data may be evidence for significant postseismic slip, although Castle *et al.* (1976) mention that preseismic dilatancy may also explain the discrepancy. It is reassuring that the moment from the static data is larger than from the dynamic data; it would be difficult to explain the opposite relationship.

Although the simple Haskell strip models of faulting can give useful time relations and rough shapes, the nucleating-dislocation model of Savage is as easy to use and is more realistic. It is limited by assumptions of being at far-field distances and of having the total rupture surface contained in a small cone of solid angle when viewed from the observation station. Both of these assumptions are commonly met for many strong-

motion recordings of moderate earthquakes. The main limitation of the method is that it assumes a uniform elastic whole-space. This limitation can be compensated for by separately modeling the effect of soil layers, by using predominately *SH* motion, and by computing takeoff angles from layered models, thus assuring that the simulated motion properly accounts for the radiation pattern.

Acknowledgments

R. P. Maley and H. Kanamori kindly supplied us with data. Adolph Oliver III, performed the numerical integrations of the accelerograms, and W. B. Joyner supplied us with the soil profile calculations. The spreading dislocation calculations were patterned after a subroutine by John Filson. Thoughtful comments on the manuscript were provided by Tom Hanks, W. B. Joyner, Allan Lindh, and Wayne Thatcher.

References

Alewine, R. W. (1974). Application of linear inversion theory toward the estimation of seismic source parameters, *Ph.D. Thesis*, California Institute Tech., Pasadena.

Anderson, J. G. (1975). Motions near a shallow rupturing fault: Evaluation of effects due to the free surface, *Trans. Am. Geophys. Union* **56,** 1027.

Boatwright, J. and D. M. Boore (1975). A simplification in the calculation of motions near a propagating dislocation, *Bull. Seism. Soc. Am.* **65,** 133–138.

Boore, D. M. and M. D. Zoback (1974). Two-dimensional kinematic fault modeling of the Pacoima Dam strong-motion recordings of the February 9, 1971, San Fernando earthquake, *Bull. Seism. Soc. Am.* **65,** 555–570.

Brune, J. N. (1970). Tectonic stress and the spectra of seismic shear waves, *J. Geophys. Res.* **75,** 4997–5009.

Burridge, R. and C. Levy (1974). Self-similar circular cracks lacking cohesion, *Bull. Seism. Soc. Am.* **64,** 1789–1808.

Carpenter, E. W. (1966). Absorption of elastic waves—an operator for a constant Q mechanism, U.K. At. Energy Authority, At. Weapons Res. Estab. *Rep. 0–43/66*, 1–16.

Castle, R. O., J. P. Church, M. R. Elliott, and J. C. Savage (1976). Preseismic and coseismic elevation changes near the epicenter of the Point Mugu earthquake of February 21, 1973 (submitted to *Bull. Seism. Soc. Am.*).

Chinnery, M. A. (1969). Theoretical fault models, in *A Symposium on Processes in the Focal Region*, K. Kasahara and A. E. Stevens, Editors, *Publ. Dominion Obs., Ottawa* **37,** 211–223.

Dosch, M. W. and W. S. Mitchell (1964). Oxnard oil field, *Calif. Div. Oil and Gas, Summ. of Operation* **50,** 21–33.

Ellsworth, W. L., R. H. Campbell, D. P. Hill, R. A. Page, R. W. Alewine, III, T. C. Hanks, T. H. Heaton, J. A. Hileman, H. Kanamori, B. Minster, and J. F. Whitcomb (1973). Point Mugu, California, earthquake of 21 February 1973 and its aftershocks, *Science* **182,** 1127–1129.

Filson, J. (1975). The sources of shallow Asian earthquakes deduced from short and long period *P* waves (abs.), *Geol. Soc. Am. Abstracts with Programs*, **7,** 405.

Gutenberg, B. (1952). SV and SH, *Trans. Am. Geophys. Union* **33,** 573–584.

Gutenberg, B. (1957). Effects of ground on earthquake motion, *Bull. Seism. Soc. Am.* **47,** 221–250.

Haskell, N. A. (1964). Total energy and energy spectral density of elastic wave radiation from propagating faults, *Bull. Seism. Soc. Am.* **54,** 1811–1842.

Haskell, N. A. (1969). Elastic displacements in the near-field of a propagating fault, *Bull. Seism. Soc. Am.* **59,** 865–908.

Hirasawa, T. (1970). Focal mechanism determinations from *S*-wave observations of different quality, *J. Physics Earth* **18,** 285–294.

Husseini, M. I., D. B. Jovanovich, M. J. Randall, and L. B. Freund (1975). The fracture energy of earthquakes, *Geophys. J.* (in press).

Joyner, W. B. and A. T. F. Chen (1975). Calculation of nonlinear ground response in earthquakes, *Bull. Seism. Soc. Am.* **65,** 1315–1336.

Kanamori, H. (1972). Determination of effective tectonic stress associated with earthquake faulting—the Tattori earthquake of 1943, *Phys. Earth Planet. Interiors* **5,** 426–434.

Kostrov, B. V. (1966). Unsteady propagation of longitudinal shear cracks, *Appl. Math. Mech.* **30,** (English transl.), 1241–1248.

Savage, J. C. (1966). Radiation from a realistic model of faulting, *Bull. Seism. Soc. Am.* **56,** 577–592.
Savage, J. C. (1972). Relation of corner frequency to fault dimensions, *J. Geophys. Res.* **77,** 3788–3795.
Stierman, D. J. and W. L. Ellsworth (1976). Aftershocks of the February 21, 1973 Point Mugu, California earthquake (submitted to *Bull. Seism. Soc. Am.*).
Thatcher, W. and T. C. Hanks (1973). Source parameters of southern California earthquakes, *J. Geophys. Res.* **78,** 8547–8576.

Department of Geophysics
Stanford University
Stanford, CA 94305

Manuscript received July 28, 1975